

The extended structure of the dwarf irregular galaxy Sagittarius^{★,★★}

G. Beccari¹, M. Bellazzini², F. Fraternali³, G. Battaglia^{2,8}, S. Perina⁴, A. Sollima², T. A. Oosterloo^{5,6},
V. Testa⁷, and S. Galletti²

¹ European Southern Observatory, Alonso de Cordova 3107, Vitacura Santiago, Chile
e-mail: gbeccari@eso.org

² INAF – Osservatorio Astronomico di Bologna, Via Ranzani 1, 40127 Bologna, Italy

³ Dipartimento di Astronomia - Università degli Studi di Bologna, Via Ranzani 1, 40127 Bologna, Italy

⁴ Department of Astronomy and Astrophysics, Pontificia Universidad Católica de Chile, Avenida Vicuña Mackenna 4860, Macul, Santiago, Chile

⁵ Netherlands Institute for Radio Astronomy, Postbus 2, 7990 AA Dwingeloo, The Netherlands

⁶ Kapteyn Astronomical Institute, University of Groningen, Postbus 800, 9700 AV Groningen, The Netherlands

⁷ INAF – Osservatorio Astronomico di Roma, via Frascati 33, 00040 Monteporzio, Italy

⁸ Instituto de Astrofísica de Canarias, 38205 La Laguna, Tenerife, Spain

Received 16 June 2014 / Accepted 6 August 2014

ABSTRACT

We present a detailed study of the stellar and HI structure of the dwarf irregular galaxy Sagittarius. We use new deep and wide field photometry to trace the surface brightness profile of the galaxy out to $\approx 5.0'$ (corresponding to ≈ 1600 pc) and down to $\mu_V \approx 30.0$ mag/arcsec², thus showing that the stellar body of the galaxy is much more extended than previously believed, and it is similarly (or more) extended than the overall HI distribution. The whole major-axis profile is consistent with a pure exponential, with a scale radius of ≈ 340 pc. The surface density maps reveal that the distribution of old and intermediate-age stars is smooth and remarkably flattened out to its edges, while the associated HI has a much rounder shape, is off-centred and presents multiple density maxima and a significant hole. No clear sign of systemic rotation is detectable in the complex HI velocity field. No metallicity gradient is detected in the old and intermediate age population of the galaxy, and we confirm that this population has a much more extended distribution than young stars (age ≤ 1 Gyr).

Key words. galaxies: dwarf – Local Group – galaxies: ISM

1. Introduction

The origin of the variety of morphologies of dwarf galaxies and the evolutionary path leading to the formation of the amorphous and gas-devoid dwarf spheroidal (dSph) galaxies have important consequences for our understanding of galaxy formation and cosmology (Mateo 1998; Tolstoy et al. 2009). The well-known fact that dSphs are found in the surroundings of large galaxies while gas-rich dwarf irregulars (dIrr) are farther away, on average, (i.e., the local morphology-density relation, see, e.g., Grcevich & Putman 2009) has led to the idea that strong interactions with the large galaxies that they are orbiting around have transformed primordial actively star-forming dIrrs into present-day quiescent dSph, removing the gas and stopping the star formation (Mateo 1998).

Recent state-of-the-art modelling in cosmological context has revealed that tidal interactions and ram-pressure stripping can be quite efficient in transforming gas-rich disc dwarfs (plunging deeply into the halo of their main galaxy) into dSphs

(the tidal stirring model, Mayer et al. 2007), but also supernova (SN) winds and the cosmic ultraviolet (UV) background are also found to play significant roles in removing gas from dwarfs (Kazantzidis et al. 2011; Sawala et al. 2010, 2012). Observations of isolated dwarfs in the Local Group (LG) are expected to provide crucial insight into the impact of the various factors on shaping the current status of dSphs, since they may represent the test case of evolution without interactions and can give insight into the initial conditions at the epoch of formation. These considerations were the driving case for a large *Hubble* Space Telescope (HST) programme (Gallart 2008) that performs extremely deep observations in small central fields of a small sample of isolated galaxies, searching for the effects of SN feedback and/or cosmic re-ionisation, since they may be recorded in the star formation history (SFH) of the systems (see, e.g., Monelli et al. 2010a,b).

We have recently started a research project aimed at exploring a fully complementary aspect, i.e., the large scale structure of these galaxies, both of their stellar body and of their gas (HI). The lack of tidal limits imposed by nearby stellar systems implies that isolated galaxies may preserve extended stellar haloes at low SB, as it has been indeed observed in some cases (e.g., Vansevičius et al. 2004, in Leo A, or Sanna et al. 2010, in IC10). This kind of feeble but extended structure (a) records crucial information on the formation and evolution of these galaxies

* Based on data obtained with the European Southern Observatory Very Large Telescope, Paranal, Chile, under the Program 089.D-0052(A).

** Table of stellar photometry (IN6) is only available at the CDS via anonymous ftp to cdsarc.u-strasbg.fr (130.79.128.5) or via <http://cdsarc.u-strasbg.fr/viz-bin/qcat?J/A+A/570/A78>

and (b) provides the precious stellar test particles to study the dynamics of these systems at large distances from their centres, thus probing their dark matter (DM) haloes over a wide radial range. The structure and kinematics of the neutral hydrogen provide additional and complementary information. It must be stressed that dwarf galaxies evolved in isolation should have preserved their pristine DM haloes virtually untouched, hence bearing fundamental information on their original structure and mass distribution.

In previous papers of this series (Bellazzini et al. 2011a, 2014, hereafter Papers I and II, respectively), we demonstrated that the outer structures of these galaxies can be traced down to extremely low surface brightness (SB) levels ($\mu_V \approx 30$ mag/arcsec²) with star counts from very deep photometry obtained with state of the art wide-field cameras on 8 m class telescopes, with modest amounts of observing time, under excellent seeing conditions. In Papers I and II we studied targets visible from the northern hemisphere, that have been observed at the Large Binocular Telescope (LBT), using the Large Binocular Camera (LBC, Giallongo et al. 2008).

In this paper we present the results of the same kind of analysis as performed with the VIMOS camera at the ESO Very Large Telescope (VLT) of our first southern target, the dwarf irregular galaxy Sagittarius (Sgr dIrr¹). Sgr dIrr is a faint star-forming galaxy (see Momany et al. 2005, hereafter M05) which is among the most gas-rich dwarfs in the local volume (Greulich & Putman 2009). It is more distant than 1 Mpc from both the MW and M31. It was independently discovered by Ciesarski et al. (1977) and Longmore et al. (1978) on photographic plates. It is located right at the edge of the LG (McConnachie 2012, M12 hereafter), and according to Teysier et al. (2012), it is likely to be falling into the LG for the first time. The most recent and detailed study of the stellar content and SFH of Sgr dIrr is that by M05, from data obtained with the Advanced Camera for Surveys (ACS) onboard the HST. Star formation has been taking place in this galaxy since ~ 10 Gyr ago (M05), with a possible significant enhancement in the star formation rate that occurred between ~ 7 and ~ 3 Gyr ago (Weisz et al. 2014).

The structure of the paper is the following. In Sect. 2 we present the observational material and we describe the data reductions and calibrations, we define the final photometric samples and present the colour-magnitude diagrams (CMD); in Sect. 3 we search for metallicity gradients among old stars and briefly consider the spatial distribution of the various stellar species. In Sect. 4 we present the SB profile and density maps. In Sect. 5 we reconsider the structure and dynamics of the HI distributions associated to Sgr dIrr, and finally, in Sect. 6 we summarise and discuss our results.

2. Observations and data reduction

Our photometric data were acquired during different nights between May 28 and July 18, 2012, using the recently refurbished VIMOS, a multi-object spectrograph and wide-field imager mounted on the Nasmyth focus B of the ESO Very Large Telescope (VLT) UT3 (Melipal). The camera is composed of four identical 4000 px \times 2000 px CCDs, each covering a field of

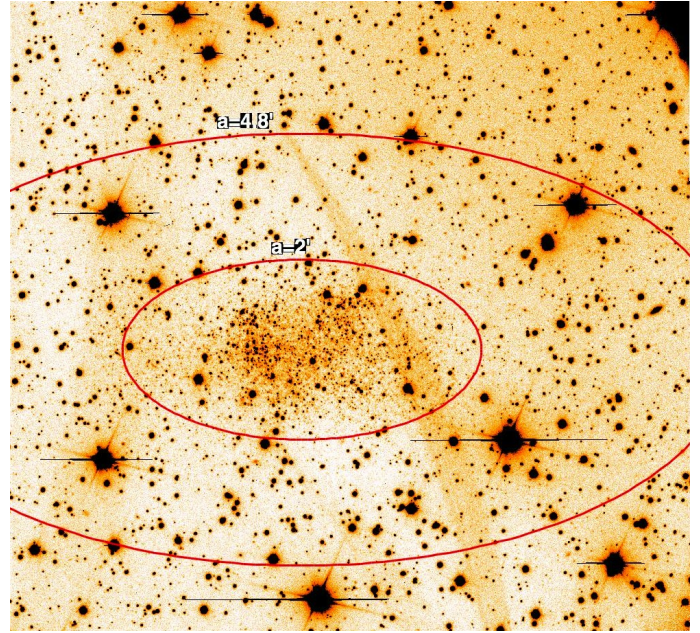


Fig. 1. Deep V band images of a VIMOS chip nearly centred on Sgr dIrr. North is up, east to the left. The two superimposed ellipses are centred on the centre of the galaxy and have the same ellipticity and PA assumed for the galaxy (see Table 1), and have semi-major axis (a) of 2' and 4.8'.

$7' \times 8'$ (pixel scale 0.205''/px), with a gap of $\sim 2'$ between each quadrant. Observations were obtained in four different pointings (P1, P2, P3, and P4, hereafter) following the scheme adopted by Correnti et al. (2011) to mosaic a continuous field (i.e., without gaps) of $\geq 20' \times 20'$. In such a scheme the centre of the galaxy is imaged in one chip in all the pointings, so that the deepest and more accurate photometry can be obtained in the central part of the galaxy. The average seeing in the four pointings was 1.3'', 1.5'', 1.1'', and 1.1'' FWHM, from P1 to P4, respectively. For each pointing, six to eight $t = 255$ s exposures per filter were acquired, in V and I.

Relative photometry was performed independently on each image using the PSF-fitting code DAOPHOTII/ALLSTAR (Stetson 1987, 1994). Sources with a peak higher than 3σ above the background were identified in a stacked image obtained by registering and co-adding all the images considered for the analysis. Then, each of these stars was re-identified and fitted on each image, when possible. To clean the catalogues from spurious sources, we also adopted cuts in the image quality parameters *CHI* and *SHARP*, provided by DAOPHOTII. After accurate inspection of the distribution of measured sources in the planes mag vs. *CHI* and mag vs. *SHARP*, we decided to retain only those sources having $CHI \leq 2.0$ and *SHARP* within magnitude-dependent contours traced to include the bulk of stellar objects, as done in Paper II.

We combined the raw photometry in two ways to obtain two different catalogues/samples:

1. The MOSAIC sample, which combines all the photometry from the four pointings to cover a field of $\approx 26' \times 22'$ as uniformly as possible.
2. The IN6 sample, which combines the repeated observations of the centre of Sgr dIrr into a field of $\approx 10' \times 8'$ with the best relative photometry and only contains sources having at least six independent magnitude estimates per filter.

¹ Other names are UKS 1927-177 and ESO 594-4. This galaxy has been sometime denoted as Sag-DIG. This name is highly unconventional since the official abbreviation for the constellation of Sagittarius is *Sgr*, not *Sag*, and the classical abbreviation for dwarf irregular is dIrr, not DIG. For this reason, we think that the name ‘‘Sag-DIG’’ should be dismissed.

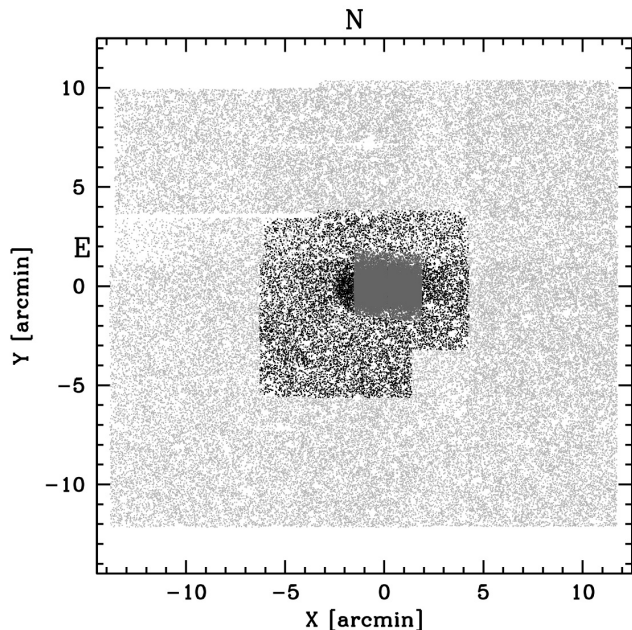


Fig. 2. Maps of the stars in the various samples. Light grey: MOSAIC sample; black: IN6 sample; dark grey: HST-ACS sample.

The sky coverage of the two samples is illustrated in Fig. 2. In the following subsections we describe in detail how these two samples have been constructed.

2.1. The MOSAIC sample

In the final catalogue of each individual chip, we retained only the sources with at least three independent magnitude estimates per filter. The average and the standard error of the mean of the independent measures obtained from the different images were adopted as the final values of the instrumental magnitude and of the uncertainty on the relative photometry. We independently transformed the x, y coordinates (in pixels) of each of these 16 subsamples (4 chips \times 4 pointings = 16 chips) into J2000 Equatorial coordinates with second degree polynomials. The transformations were obtained by model fitting to 300–800 stars in common between each chip and the GSC2.2² catalogue of astrometric standards, with a typical rms of $\leq 0.25''$ in each coordinate³. Then all the individual catalogues were moved into a common relative photometry system using the stars in common in the overlapping areas between chips of different pointings. Finally all the catalogues of the individual chips were merged. Magnitudes and positions of stars in common between different

² The Guide Star Catalogue-II is a joint project of the Space Telescope Science Institute and the Osservatorio Astronomico di Torino. Space Telescope Science Institute is operated by the Association of Universities for Research in Astronomy, for the National Aeronautics and Space Administration under contract NAS5-26555. The participation of the Osservatorio Astronomico di Torino is supported by the Italian Council for Research in Astronomy. Additional support is provided by European Southern Observatory, Space Telescope European Coordinating Facility, the International GEMINI project and the European Space Agency Astrophysics Division.

³ All the astrometric solutions presented here have been obtained with CataXcorr, a code developed by P. Montegriffo at INAF – Osservatorio Astronomico di Bologna, and successfully used by our group during the past 10 years. See <http://davide2.bo.astro.it/~paolo/Main/CataPack.html>

chips were taken from the best dataset, adopting the following hierarchy: P3, P4, P1, P2. In this way each star in the MOSAIC catalogue has its magnitudes (and associated errors) obtained from three independent estimates per filter, independently of its position in the field, thus ensuring the highest level of homogeneity attainable over the widest field that can be covered with our data. Inspection of Fig. 2 reveals that the various degrees of overlap between different chips, the variations in mean seeing between different pointings, and the presence of heavily saturated bright foreground stars in the field introduces some degree of inhomogeneity in the MOSAIC sample. Still this is the most uniform sample on the widest field that we can obtain from the available observational material. We refined the global astrometry of the MOSAIC catalogue as a whole with a fourth degree polynomial fitted to the 7042 stars in common with GSC2.2. The final rms is $\approx 0.23''$ in each coordinate. We use the MOSAIC sample in Sect. 4 to trace the full extension of the stellar body of Sgr dIrr.

2.2. The IN6 sample

In this case DAOPHOT/ALLFRAME was forced to produce an output catalogue containing only sources with at least *six* independent magnitude estimates per filter. This strong requirement limits the global FoV covered by the IN6 sample to an inner region that maximises the overlapping between chips from different pointings (see Fig. 2). The average and the standard error of the mean of the independent measures obtained from the different images were adopted as the final values of the instrumental magnitude and of the uncertainty on the relative photometry. The large number of independent magnitude estimates combined imply a significantly higher precision of the relative photometry with respect to the MOSAIC sample, as is evident from Fig. 3. Also in this case the instrumental coordinates were transformed into J2000 Equatorial coordinates with second degree polynomials, using more than 1000 stars in common with the GSC2.2 catalogue. The r.m.s of the fits is $\leq 0.23''$ in each coordinate. We use the IN6 catalogue in Sect. 3 to study the metallicity and population gradients in Sgr dIrr, and in Sect. 4 to validate the structural analysis performed with the MOSAIC sample. We make the IN6 Catalog publicly available at the CDS.

2.3. Photometric calibration

The instrumental magnitudes (v, i) of both samples were transformed into the Johnson-Kron-Cousins V, I photometric system (Landolt 1992) using more than 70 bright stars ($V < 22.5$) in common with the publicly available HST Wide Field and Planetary Camera 2 (WFPC2) photometry by Holtzman et al. (2006)⁴, with first-order polynomials as a function of $v - i$ for the I band, and with a simple zero point (ZP) correction for the V band. The transformations were optimised for the colour range spanned by stars of the target galaxy ($-0.5 \lesssim V - I \lesssim 2.0$).

We compared our final calibrated photometry with that by Lee & Kim (2000, LK00, hereafter), who provide B, V, R, I magnitudes for a subsample of stars brighter than $V = 20.8$. The mean difference between the two photometries is less than 0.01 in V from 85 stars in common, while it is larger than 0.2 in I with a significant dependence on colour. The comparison with the HST-ACS photometry presented below strongly suggests that our I photometry is more correct than it is in LK00.

⁴ <http://astronomy.nmsu.edu/holtz/archival/html/lg.html>

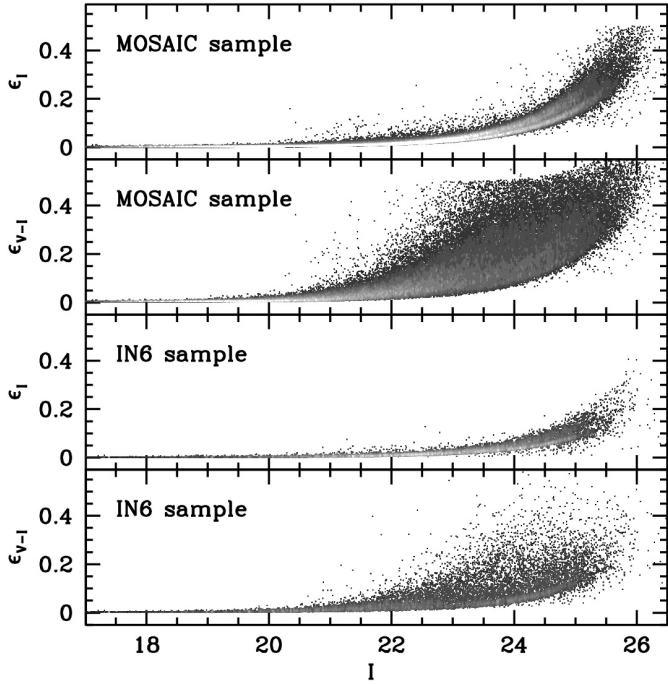


Fig. 3. Distribution of photometric errors in magnitude and colours for the two samples, MOSAIC (*upper two panels*), and IN6 (*lower two panels*). Stars are plotted as black points in regions of the diagrams with a few stars and as grey squares otherwise, with the scale of grey proportional to the local density. Lighter tones of grey correspond to higher density.

2.4. HST-ACS photometry

From the HST archive we retrieved the F606W and F814W images of Sgr dIrr from the Program GO 9820, i.e. part of the observational material used by M05. PSF photometry on the pre-reduced images was performed with the ACS module of DOLPHOT (Dolphin 2000), exactly in the same way as described in detail in Bellazzini et al. (2011b). As in that analysis, we only selected stars with the best quality flag (`obj_type=1`), $CHI < 2.0$, $|SHARP| < 0.5$, crowding parameter < 0.3 , and photometric error < 0.3 mag, in both filters. These cuts produced a cleaned catalogue with 24911 sources. DOLPHOT automatically provides calibrated magnitudes, also in the Johnson-Kron-Cousins system that we adopt here. The final CMD is very similar to that obtained by M05 (see Fig. 6, below). The instrumental coordinates were transformed into J2000 equatorial coordinates with third degree polynomial, using more than 3300 stars in common with the IN6 catalogue. The rms of the fits is $\leq 0.05''$ in each coordinate. The position of the ACS sample with respect to the two VIMOS samples is illustrated in Fig. 2.

2.5. Reddening and distance

We interpolated the Schlegel et al. (1998) reddening maps – as re-calibrated by Schlafly & Finkbeiner (2011) – to obtain an estimate of $E(B - V)$ and its variation over the MOSAIC FoV. We adopted a regular grid with knots spaced by $2.0'$, finding (a) a mean reddening values slightly lower than those usually reported in the literature (see, e.g., M05, M12) due to the Schlafly et al. re-calibration, and (b) that the reddening variations are negligible for our purposes (see Table 1; see M05 for a discussion of the effect of differential reddening on the youngest stars). In

the following, we adopt the reddening laws $A_V = 3.1E(B - V)$ and $A_I = 1.76E(B - V)$ from Dean et al. (1978).

To obtain distances fully consistent with the scale adopted in Papers I and II we used our newly derived V, I ACS-HST photometry to (a) correct the CMD for the newly derived values of the reddening, and (b) derive the magnitude and mean colours of the RGB-Tip again, as done in Papers I and II. We obtain $I_{0,\text{tip}} = 21.10 \pm 0.04$ and $(V - I)_{0,\text{tip}} = 1.27$, in excellent agreement with M05 (taking also into account the slight difference in the adopted reddening). Using the relation for the absolute magnitude of the RGB Tip already adopted in the previous papers of this series:

$$M_I^{\text{TRGB}} = 0.080(V - I)_0^2 - 0.194(V - I)_0 - 3.939 \quad (1)$$

from Bellazzini (2008), we obtain $M_I^{\text{TRGB}} = -4.06 \pm 0.10$. Finally, we obtain $(m - M)_0 = 25.16 \pm 0.11$, corresponding to $D = 1076 \pm 55$ kpc, where the reported errors include *all the statistical and systematic sources of error*. The derived distance estimate is in excellent agreement with M05 and M12.

2.6. Surface photometry and coordinate system

As a basis for constructing the final composite profiles (surface photometry + star counts; see Sect. 4), we adopted the surface photometry by LK00. We also adopted the ellipticity (ϵ) and position angle (PA) estimated by LK00, since we verified that they are appropriate over the whole radial range where we detect Sgr dIrr stars (see Sect. 4 below).

Adopting the coordinates for the centre listed in Table 1, we converted the equatorial coordinates of each star (α, δ) to cartesian coordinates X, Y (in arcmin) on the plane of sky as done in Paper I, with X increasing towards the west and Y increasing towards the north. Finally, we defined the elliptical distance from the centre of the galaxy (or elliptical radius r_ϵ) as

$$r_\epsilon = \sqrt{X^2 + \left(\frac{Y}{1 - \epsilon}\right)^2}$$

which is equivalent to the major-axis radius. The X, Y coordinate system and r_ϵ will always be adopted in the following analysis.

2.7. The colour–magnitude diagrams

In Fig. 4 we present our final CMD in different radial ranges for the MOSAIC sample. Our photometry reaches $I \sim 25.5$, thus sampling the extended red clump (RC) of Sgr dIrr. The CMDs is dominated by a strong and (relatively) wide red giant branch (RGB), ranging from $(I, V - I) \sim (25.5, 0.8)$ to $\sim (21.5, 1.5)$. The population of He-burning stars extends from the RC up to $(I, V - I) \sim (19.5, 0.0)$ into a blue loop (BL) sequence. The young main sequence (MS) plume at the blue edge of the CMDs runs parallel to the BL sequence (and partially overlapping it, in colour) up to $I \sim 21$. The sparse sequence of red super giants (RSG) is barely visible, on the blue side of the RGB and parallel to it for $I \lesssim 22.5$ (see M05 for a detailed description of the various evolutionary sequences that can be identified in the ACS CMD).

The middle panel of Fig. 4 clearly demonstrates that Sgr dIrr stars are present in a (relatively) large number beyond the radial range covered by existing surface photometry ($r_\epsilon \approx 2'$, where $\mu_V \approx 26.3$ mag/arcsec², see LK00 and Fig. 10, below). The right-hand panel of the figure shows the fore/background population that contaminates our CMDs. Given the relatively low

Table 1. Observed and derived parameters of Sagittarius dIrr.

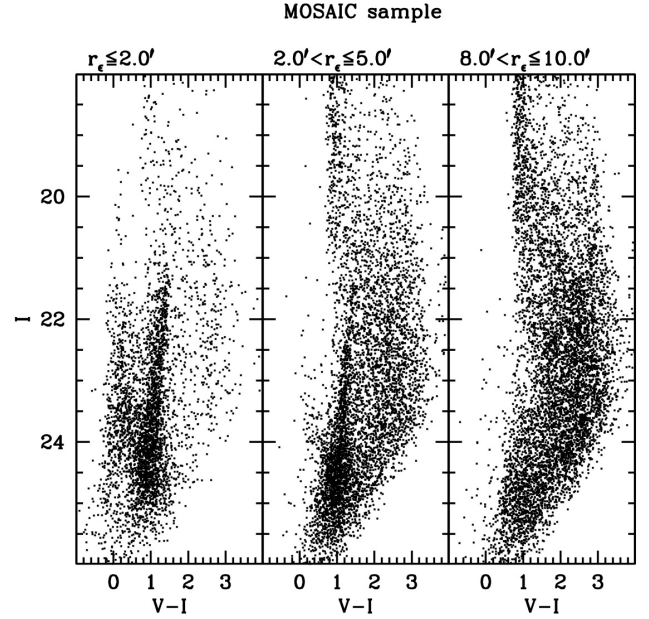
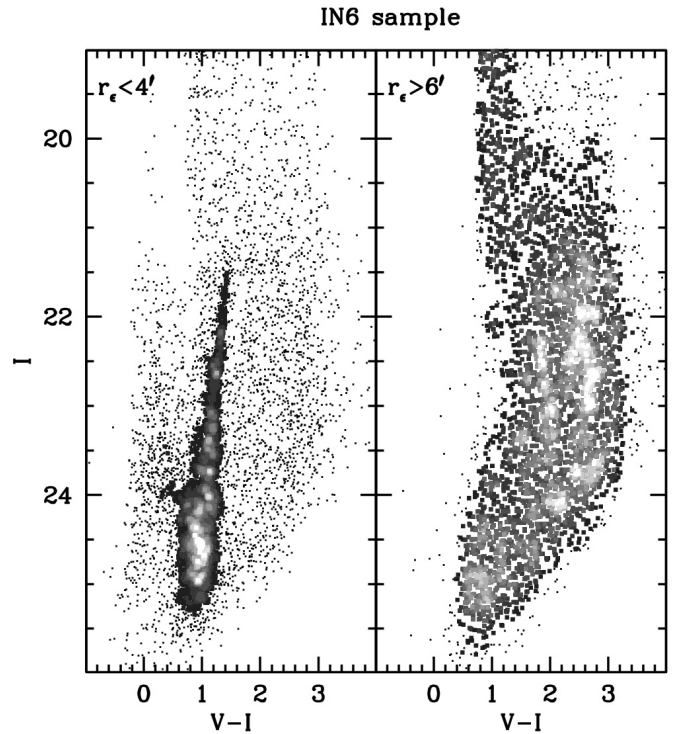
Parameter	Value	Notes
α_0	19:29:59.9	J2000 ^a
δ_0	-17:40:49.4	J2000 ^a
l_0	21.055°	Gal. long.
b_0	-16.289°	Gal. lat.
SGL	221.275°	Supergal. long.
SGB	55.516°	Supergal. lat.
$E(B - V)$	0.107 ± 0.010	Average $\pm \sigma^b$
$(m - M)_0$	25.16 ± 0.11	
D	1076 ± 55 kpc	
1 arcsec	5.2 pc	conv. factor at $D = 1076$ kpc
V_h	-78.5 ± 1 km s ⁻²	heliocentric velocity ^c
V_g	8 km s ⁻¹	galactocentric velocity ^c
$\langle [\text{Fe}/\text{H}] \rangle$	-2.0	from RGB colour ^d
ϵ	0.50	from LK00
PA	90°	from LK00
$\mu_V(0)$	23.9 ± 0.1 mag/arcsec ²	central SB ^e
h	1.1'	Sérsic scale radius
r_h	1.1'	Observed ^f
V_{tot}	13.4 ± 0.1	Observed ^f
M_V	-12.1 ± 0.2	
L_V	$5.8^{+1.1}_{-1.0} \times 10^6 L_{V\odot}$	total V luminosity
M_{HI}	$8.7 \times 10^6 M_\odot$	HI mass ^g

Notes. ^(a) Estimated by eye from HST-ACS images and verified to provide a more satisfactory centre of symmetry for the distribution of RGB stars w.r.t. the centre listed by M12. Our new centre is 13.5'' to the east and 9.4'' to the south of the M12 centre. ^(b) Average over the whole FoV from the reddening maps by Schlegel et al. (1998), as recalibrated by Schlafly & Finkbeiner (2011) (regular grid covering the whole MOSAIC field with knots spaced by 2'). ^(c) From McConnachie (2012). ^(d) From the HST-ACS sample, see Sect. 3. ^(e) μ_V of the innermost point of the observed profile. Not corrected for extinction. The central SB of the best fitting Sersic profile is $\mu_V(0) = 23.3$ mag/arcsec². ^(f) From the numerical integration of the SB profile in r_ϵ . V_{tot} is in excellent agreement with the integrated magnitude of the best-fit Sersic model, $V_{\text{tot}} = 13.3$. ^(g) From Hunter et al. (2012).

angular distance both from the Galactic centre and plane, the contamination from foreground Galactic stars is particularly severe, e.g., with respect to the high latitude galaxies studied in Papers I and II. The vertical plume spanning the whole diagram around $V - I \sim 3.0$ is due to local M dwarfs; the sparse wide band around $V - I \sim 1.0$, bending to the red for $I \gtrsim 22.0$, is due to foreground MS stars in the Galactic thick disc and halo; while the broad blob of sources with $0.0 \lesssim V - I \lesssim 2.0$ and $I \gtrsim 23.0$ is largely dominated by distant unresolved galaxies (see Paper I for a detailed discussion and references).

In Fig. 5 the CMDs for two large radial ranges of the IN6 sample is presented as a greyscale Hess diagram (as in Bellazzini et al. 2011b). Some features are more clearly seen in this diagram, such as the density peak of the RC and a weak overdensity above the RGB Tip that may trace the AGB population identified by M05 and Gullieuszik et al. (2007).

In Fig. 6 we provide a direct comparison between VIMOS (IN6) and HST-ACS photometry. In the upper panels, it is shown that the photometric ZPs are in reasonable agreement. The lower panels display the CMDs obtained from the two datasets for the stars in common. Clearly our ground based photometry cannot rival the top-level quality achievable from the space, especially in the highly crowded central regions sampled by the HST data. Still, it is remarkable that virtually all the features that can be identified in the VIMOS CMDs have clear counterparts in the


Fig. 4. CMDs in different radial ranges from the MOSAIC sample.

Fig. 5. CMDs in different radial ranges from the IN6 sample. Stars are plotted as black points in regions of the CMD with a few stars and as grey squares, otherwise with the scale of grey proportional to the local density in the CMD. Lighter tones of grey correspond to higher density.

HST CMDs, thus indicating that the precision of our photometry is sufficient to reliably distinguish stars in different evolutionary phases.

3. Metallicity and population gradients

In Fig. 7 we compare the observed RGB from the HST-ACS sample in two radial ranges covered by these data with a grid of RGB ridge lines of Galactic globular clusters (GC). The ridge

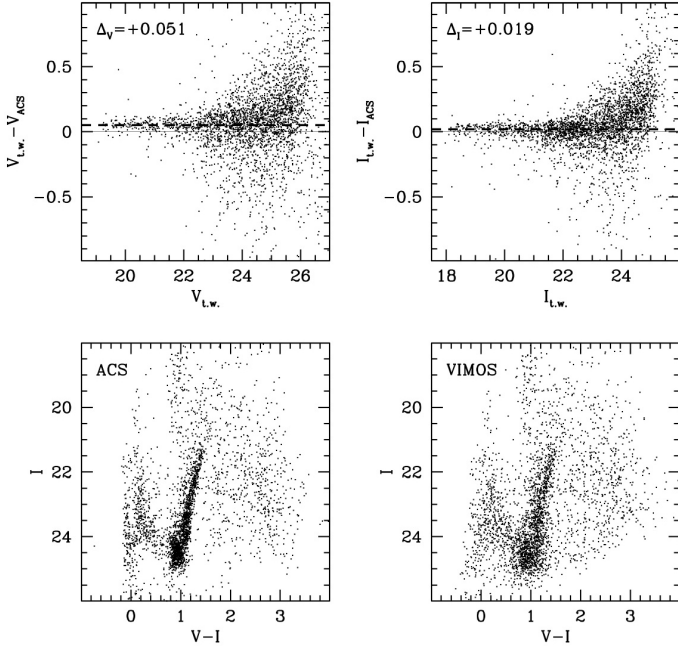


Fig. 6. Comparison between HST-ACS and VLT-VIMOS photometry. *Upper panels:* comparison of the photometric zero points. *Lower panels:* CMDs for the stars in common between the two datasets.

lines are taken from the homogeneous set by Saviane et al. (2000); the adopted reddening and distance of the clusters are from Ferraro et al. (1999). The template clusters are NGC 6341, NGC 5275, and NGC 288, from left to right; the associated metallicities are $[\text{Fe}/\text{H}] = -2.31, -1.50,$ and $-1.32,$ respectively, from the December 2010 version of the Harris (1996) catalogue. In both CMDs the $[\text{Fe}/\text{H}] = -2.31$ template lies straight in the middle of the bulk of RGB stars, and there is no hint of a difference in the RGB colours in the considered radial ranges. Interpolating on this grid of RGB templates (as done in Papers I and II, following Bellazzini et al. 2002b) for RGB stars within two magnitudes from the tip (and neglecting the effects of field contamination, which should be very weak for this sample), we obtain a mean metallicity $\langle [\text{Fe}/\text{H}] \rangle = -2.0$ with a standard deviation $\sigma_{[\text{Fe}/\text{H}]} = 0.37,$ in good agreement with M05 (see also Momany et al. 2002, and references therein). While there is no doubt that the galaxy is dominated by very metal-poor stars (see, e.g. Saviane et al. 2002, and references therein, for the metallicity of H II regions), the derived mean should be regarded as a lower limit to the mean metallicity, since the observed RGB is also significantly populated by stars that are a few Gyr younger than the GC templates (see Paper II for a detailed discussion of the analogous case of Sex A). The presence of intermediate-age populations in Sgr-dIrr is demonstrated by the morphology of the red clump and by the presence of bright AGBs and carbon stars (see Gullieuszik et al. 2007, and references therein). Photometric estimates of the mean metallicity in these distant stellar systems with extended star formation should always be considered as educated guesses.

We extend the search for a metallicity gradient to larger elliptical radii using the IN6 sample. In Fig. 8 we compare the CMDs for four different radial ranges, reaching the outer limit of Sgr dIrr ($r_\epsilon = 4.0'$, see Sect. 4, below) with the same grid of RGB templates used in Fig. 7. We removed the ridge line of NGC 5272, for clarity. In the innermost radial range, the effects of crowding are too severe to allow a meaningful comparison. On the other hand, the results from the HST-ACS and IN6

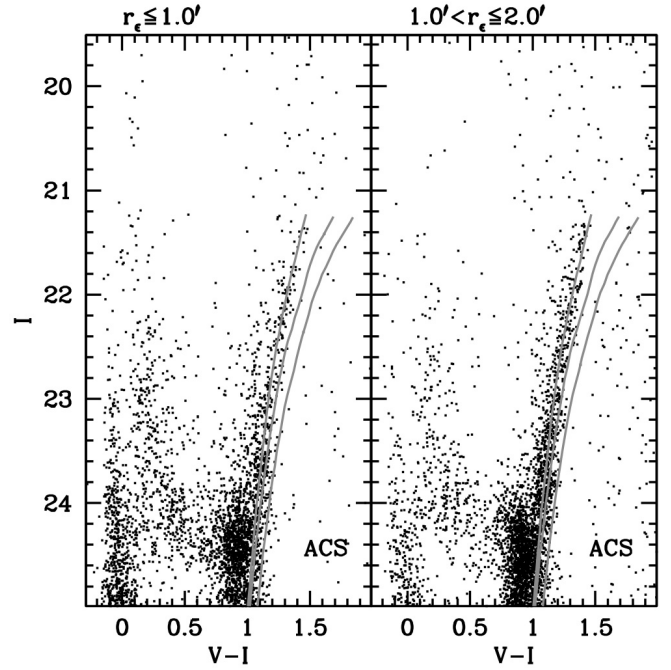


Fig. 7. CMDs zoomed on the RGB for two radial ranges, from the HST-ACS sample. The ridge lines of the clusters NGC 6341, NGC 5275, and NGC 288, from left to right, from the set by Saviane et al. (2000) have been superimposed, after shifting them to reddening and distance of Sgr dIrr. According to the December 2010 version of the Harris (1996) catalogue, the metallicity values corresponding to the three ridge lines are $[\text{Fe}/\text{H}] = -2.31, -1.50,$ and $-1.32,$ respectively.

samples for the range $1.0' < r_\epsilon \leq 2.0'$ are fully compatible. From Figs. 7 and 8 we can conclude that we do not detect any sign of a metallicity gradient in the RGB population over the whole body of the Sgr dIrr galaxy.

In the lower panel of Fig. 9, we compare the radial distribution of RGB and MS+BL stars, selected with the boxes illustrated in the upper panel of the same figure. The analysis is limited to stars in the same range of magnitude, for stars ~ 2 mag above the limits of the photometry, to compare samples that are equally affected by incompleteness. As is typical of dwarf galaxies, the backbone of old-to-intermediate-age stars has a much more extended distribution than populations younger than 1 Gyr, as traced by MS+BL stars. Figure 9 shows that $\sim 90\%$ of MS+BL stars are confined within $r_\epsilon = 2.0'$, a region that is largely covered by the HST-ACS sample. For a detailed analysis of this population and of its spatial distribution in relation with the distribution of H I, we refer the interested reader to the extensive discussion by M05.

Finally, M05 notes a gap in luminosity in the brightest part of the BL sequence (between $I = 21.1$ and $I = 20.6$ in Fig. 7), which may trace a short quiescent phase in the star formation that occurred some 2–60 myr ago. Unfortunately, the population on the bright side of the gap is constituted by a handful of stars, so it is difficult to firmly assess the statistical significance of this feature. In this context, it is interesting to note that the same gap is clearly detected in our own ground-based photometry, in particular when the IN6 sample is considered (see Fig. 5), thus providing additional support to a scenario of intermittent star formation in the past 100 Myr, which might also be associated to the inhomogeneities in the distribution and velocity field of the H I (see Sect. 5).

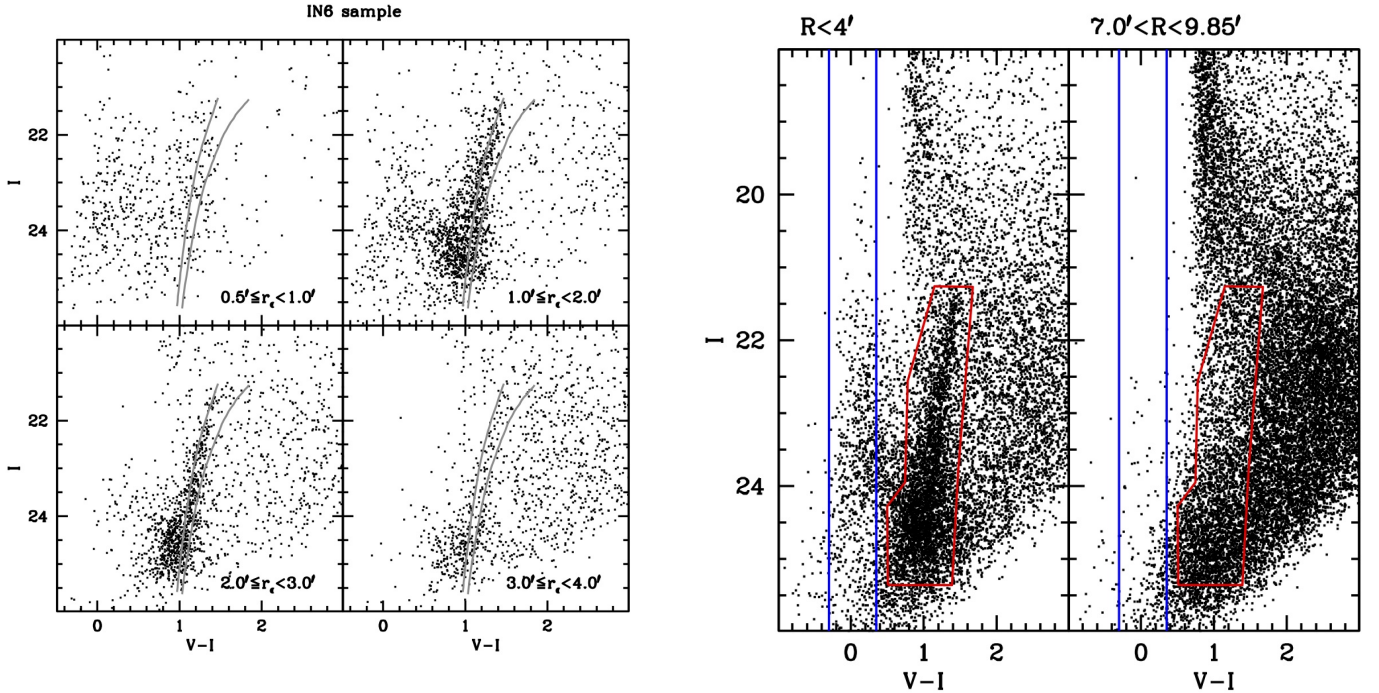


Fig. 8. CMDs zoomed on the RGB for four radial ranges, from the VIMOS IN6 sample. The ridge lines of the clusters NGC 6341 and NGC 288, from *left to right*, from the set by Saviane et al. (2000) have been superimposed, after shifting them to reddening and distance of Sgr dIrr.

4. Structure

In Fig. 10 we show the azimuthally-averaged surface brightness (SB) profile of Sgr dIrr. The profile was obtained by joining the V -band surface photometry from LK00 out to $r_\epsilon = 1.83'$, with the surface density profile obtained from star counts in elliptical annuli, while keeping the values of ϵ and PA derived in Sect. 2.6 fixed. The (large) overlapping region between the profiles from surface photometry and from star counts was used to normalise the star-count profile, shifting it to the V magnitude scale of the surface photometry profile.

For the star counts we used as homogeneous density tracers, candidate RGB stars enclosed in the polygonal box which is shown in the upper panel of Fig. 9. The background was estimated in wide areas at $r_\epsilon > 8'$. The profiles were constructed starting with bright magnitude limits in the inner regions and going to fainter limits in the outskirts to get rid of variations in the completeness with distance from the galaxy centre and to have the highest SB sensitivity in the low-SB external regions, as described in detail in Paper II.

As in the cases presented in previous papers of this series, our newly derived composite profile reaches much larger radii (by a factor of ≥ 2) than previous studies, which were based solely on surface photometry. In particular, we are able to trace the stellar profiles out to $r_\epsilon \approx 4.7'$, showing that this galaxy is also much more extended than what previously observed (see Papers I and II, and references therein).

In general, the overall profile is well fitted by a single Sérsic (1968) model⁵ with $n = 1.0$, i.e. a pure exponential, as is typical

⁵ Here we adopt the formalism by Ciotti & Bertin (1999), with the SB profile given by $I(r) = I_0 e^{-b\eta^{\frac{1}{n}}}$ (their Eq. (1)), with $\eta = \frac{r}{h}$, h being the half-light radius. The value of the constant b is from their Eq. (25), which works well for $n \geq 1.0$.

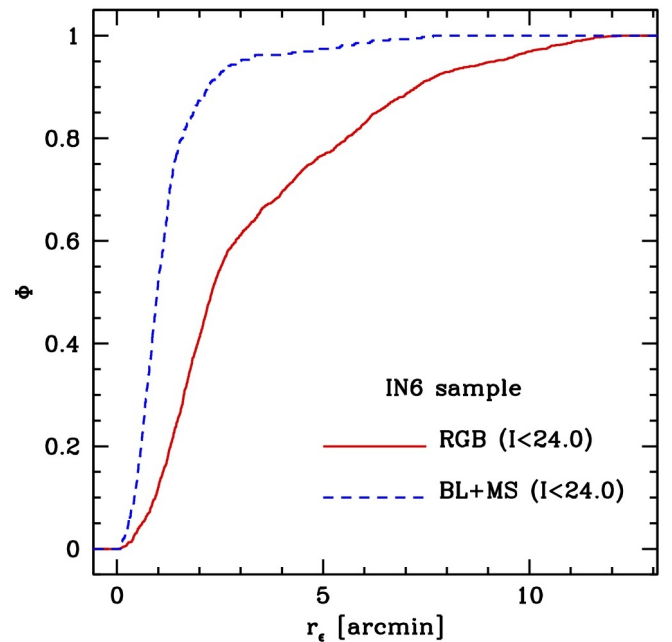


Fig. 9. Upper panel: selection boxes for BL+MS stars and RGB stars are superimposed to CMDs representative of the Sgr dIrr galaxy (*left panel*) and of the fore/background contaminating field (*right panel*), from the MOSAIC sample. The colour range adopted to select BL+MS stars is $-0.30 < V - I < 0.35$. Note that the *field* CMD samples an area that is exactly three times of that sampled by the *on target* CMD. Lower panel: cumulative radial distribution of the BL+MS (dashed blue line) and RGB (continuous red line) populations in the same range of magnitude.

of low luminosity dwarfs (Mateo 1998). For $r_\epsilon \geq 2'$ the profile from star counts present some weak kinks and weaves (with a hint of an external flattening of the slope) that we do not regard as significant, since small-scale asymmetries (both real and/or associated to holes due to heavily saturated foreground stars) can be the origin of these features in the low SB realm considered

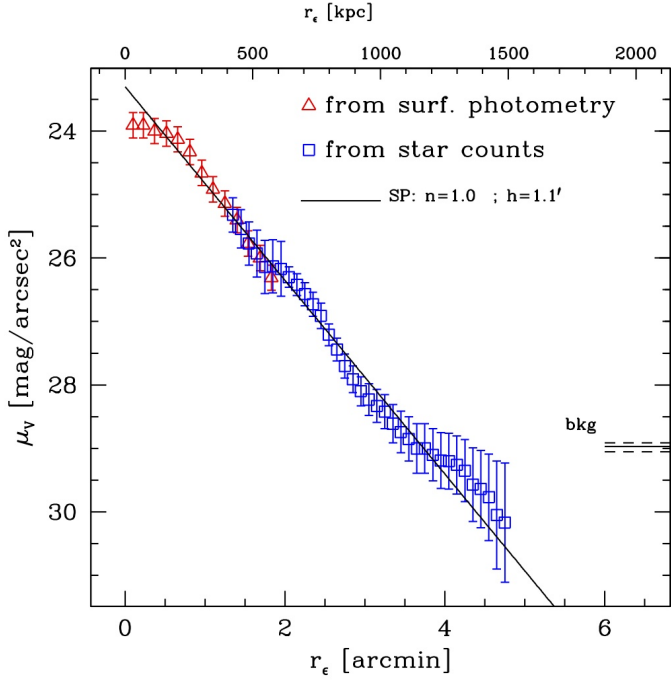


Fig. 10. Surface brightness profile of Sgr dIrr in V band obtained by joining surface photometry from LK00 (open triangles) and star count (open squares) profiles. The continuous line is the Sersic model that best fits the profile. The level of the background (bkg) and the associated uncertainty is also reported.

here. The flattening in the innermost ~ 200 pc is very similar to what is observed in the profile of Sextans B (Paper II).

Integrating the profile shown in Fig. 10 numerically, we obtain integrated V magnitudes $V_{\text{tot}} = 13.4 \pm 0.1$, and half-light radii $r_h = 1.1'$, in excellent agreement with the respective values for the best-fitting exponential model and in reasonable agreement with the values reported in the literature (M12), which are based on much less extended observed profiles.

4.1. Density maps

In Fig. 11 we present the density map for Sgr dIrr obtained with the MOSAIC sample from RGB star counts (selected as for the SB profile) on a fixed regular grid of nodes spaced by $0.1'$, with the same adaptive algorithm described in Papers I and II. The lightest tone of grey corresponds to an over-density at 3σ above the background level, and it is the outermost density contour that we can reliably trace with our data. All the RGB stars selected for the analysis are also plotted in the maps to give an idea of the sampling biases that are obviously affecting them (inter-chip gaps, saturated stars, etc.). Single isolated weak peaks with typical scales $\lesssim 1'$ can correspond to clusters of galaxies whose red sequence galaxies fall in the RGB selection box or to clumping of spurious sources in the haloes of heavily saturated stars. We note, however, that we were unable to associate the wide blob centred at $(X, Y) \sim (6.5, 0.5)$ with any obvious clustering of galaxies in the deep stacked images. It therefore cannot be excluded that the stellar distribution of Sgr dIrr may extend even beyond $X \sim 5'$, at surface brightness levels $\mu_V \gtrsim 30.0$ mag/arcsec 2 .

The stellar body of Sgr dIrr (as traced by intermediate-to-old stars) is made up of an inner boxy component, out to $r_\epsilon \simeq 2.0'$, surrounded by a more elongated halo, somehow resembling a

Table 2. Observed surface brightness profile.

r_ϵ	μ_V	Source
arcmin	mag/arcsec 2	
0.10	23.91 ± 0.10	LK00
0.23	23.91 ± 0.10	LK00
0.37	24.00 ± 0.10	LK00
0.52	24.04 ± 0.10	LK00
0.66	24.13 ± 0.10	LK00
0.81	24.33 ± 0.10	LK00
0.96	24.66 ± 0.10	LK00
1.10	24.92 ± 0.10	LK00
1.25	25.14 ± 0.10	LK00
1.40	25.40 ± 0.10	LK00
1.54	25.77 ± 0.10	LK00
1.69	26.00 ± 0.10	LK00
1.83	26.31 ± 0.10	LK00
1.95	26.17 ± 0.43	sc
2.05	26.30 ± 0.16	sc
2.15	26.42 ± 0.17	sc
2.25	26.57 ± 0.18	sc
2.35	26.73 ± 0.19	sc
2.45	26.91 ± 0.20	sc
2.55	27.21 ± 0.17	sc
2.65	27.44 ± 0.18	sc
2.75	27.70 ± 0.19	sc
2.85	27.91 ± 0.21	sc
2.95	28.10 ± 0.23	sc
3.05	28.23 ± 0.25	sc
3.15	28.33 ± 0.26	sc
3.25	28.42 ± 0.27	sc
3.35	28.61 ± 0.30	sc
3.45	28.74 ± 0.33	sc
3.55	28.85 ± 0.35	sc
3.65	29.00 ± 0.39	sc
3.75	29.00 ± 0.39	sc
3.85	29.10 ± 0.41	sc
3.95	29.19 ± 0.44	sc
4.05	29.20 ± 0.44	sc
4.15	29.26 ± 0.46	sc
4.25	29.35 ± 0.49	sc
4.35	29.57 ± 0.58	sc
4.45	29.64 ± 0.61	sc
4.55	29.77 ± 0.68	sc
4.65	30.05 ± 0.85	sc
4.75	30.17 ± 0.94	sc

Notes. LK00 = surface photometry from LK00; sc = star counts from the present analysis. Since LK00 do not provide uncertainties, we assume 0.1 mag for their estimates. Not corrected for extinction.

thick disc seen nearly edge-on (see Paper I). This impression is confirmed by the map shown in Fig. 12 obtained with the matched filter technique (see Rockosi et al. 2002, and Paper I) from the IN6 sample, which is much less affected by discontinuities in the spatial sampling or by spurious sources than the MOSAIC sample.

It is interesting to note that the correlation with the distribution of H I (superimposed contours obtained from LITTLE THINGS data Hunter et al. 2012; see Sect. 5) is relatively poor. The H I cloud associated to Sgr dIrr has a size comparable to the stellar body, but its outer contours have a much rounder shape and irregular structure; the density peak is significantly off-centred with respect to the centre of symmetry of the stellar body.

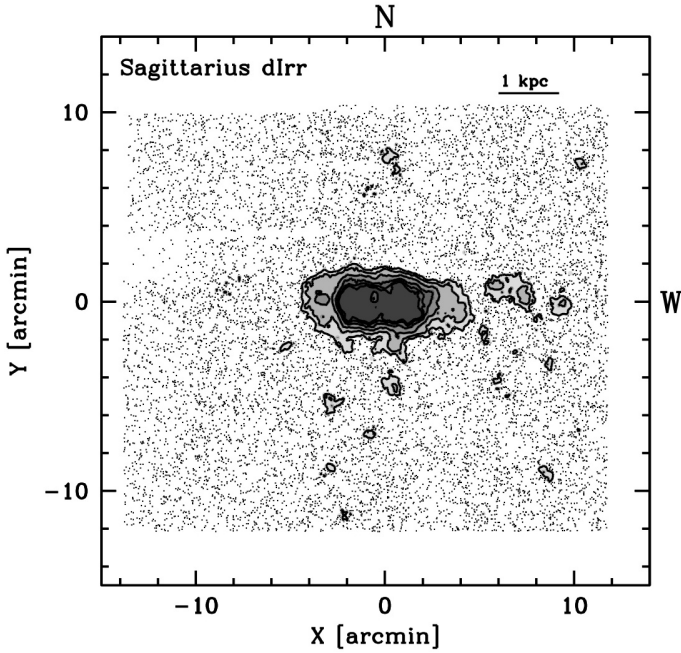


Fig. 11. Density map obtained from RGB star counts. The levels of grey correspond to density of 3, 5, 10, 20, 40, and 80σ above the background, from the lightest to the darkest tone of grey. All the RGB stars falling in the selection box defined in Fig. 9 are also plotted (as dots) to provide a direct illustration of the effects of the footprint of the mosaic.

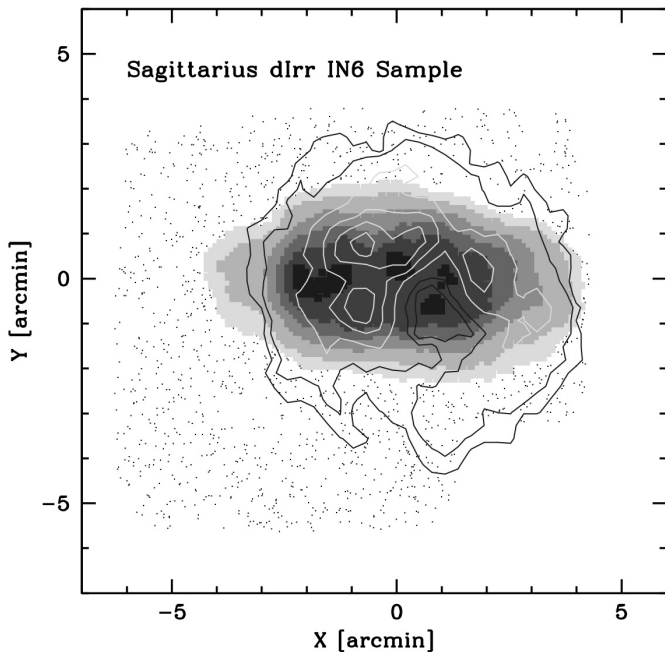


Fig. 12. Density map obtained with the matched filter technique from the IN6 sample. The symbols are the same as in Fig. 11. A higher level of smoothing has been adopted. The HI column density contours obtained from LITTLE THINGS data (with a beam of $28.2'' \times 16.9''$) were superimposed. The associated density is 0.5, 1.0, 3.0, 5.0, 7.0, $9.0 \times 10^{20} \text{ cm}^{-2}$, from the outermost to the innermost contour.

5. Neutral hydrogen

We analysed the HI data cubes for Sgr dIrr made publicly available from the LITTLE THINGS Survey (Hunter et al. 2012)

using the Groningen Image Processing SYstem (GIPSY)⁶. We first smoothed the HI data cube to a resolution of $30'' \times 30''$ and produced a new total HI map and velocity field. We built the total HI map by adding up the emission after the application of a mask to each channel. The mask was created by smoothing the original cube to a resolution of $60''$ and eliminating the regions with fluxes below $+2.5\sigma_{60''}$, where $\sigma_{60''}$ is the rms noise of the smoothed cube. We derived a total HI mass of $\sim 8 \times 10^6 M_{\odot}$, in excellent agreement with what was found by Hunter et al. (2012) from the same data. Figure 13 (left panel) shows the total HI map (contours) of Sgr dIrr in greyscale and contours. The shape of the gas distribution is almost perfectly round with an inner depletion slightly off-set with respect to the optical centre (see also Fig. 12). This depletion may have been caused by intense star formation and be the sign of either gas removal or ionisation.

The overall HI kinematics can be appreciated from the velocity field in the right-hand panel of Fig. 13, derived using the first moment of the line-of-sight velocity distribution. The kinematics is complex, and there seems to be no clear pattern of rotation or a systematic segregation of blue-shifted and red-shifted regions (see also Young & Lo 1997). To test the possible presence of low-level rotation, we extracted a position-velocity ($p-v$) diagram from the data cube along the major axis of the stellar distribution. Figure 14 shows this $p-v$ plot and confirms the lack of any obvious velocity gradient. Should one interpret the slight dislocation of the upper contours in Fig. 14 as rotation, that would yield $v_{\text{rot}} \sim 2 \times \frac{\sin(60^\circ)}{\sin(i)}$ km s⁻¹. In an irregular system such as Sgr dIrr, it is possible that the gas rotation is not aligned with the optical major axis (e.g., Lelli et al. 2014). Thus, we checked for rotation along other directions but found only a slight gradient for angles close to the optical minor axis that is more likely associated with outflow/inflow motions of the gas (Battaglia & Fraternali, in prep.).

The lack of a rotational signal in Sgr dIrr can have different interpretations. One possibility is that a rotation of a few km s⁻¹ may go undetected because it is lower than the HI velocity dispersion, ranging from ~ 5 to more than 10 km s⁻¹. The HI gas may also have a somewhat spherical and potentially pressure-supported distribution or, if a disc is present, it may have an inclination close to face-on, compatible with the projected round shape, which would make any line-of-sight rotational component very weak. Finally, recent episodes of star formation may locally increase the non-circular motions of the HI gas and make the signature of rotation temporarily undetectable.

The global HI velocity profile of Sgr dIrr can be fitted with a single Gaussian function with velocity dispersion $\sigma_{\text{HI}} = 8.6 \pm 0.1 \text{ km s}^{-1}$. In the inner regions, where the density is higher, the line profiles appear more complex, and a single Gaussian does not return a very good fit. Considering two Gaussian functions, we find values of about 5 and 10 km s⁻¹ for the narrow and broad components, respectively. This maybe be the same indication of two-phase interstellar medium as seen in other dwarf galaxies (e.g., Young & Lo 1997; Ryan-Weber et al. 2008), including VV124 (Paper I).

Given the lack of rotation, it is difficult to reliably estimate the dynamical mass of Sgr dIrr. However, we can derive an order-of-magnitude estimation using the average observed HI velocity dispersion $\sigma_{\text{HI}} \simeq 8.6 \text{ km s}^{-1}$. Assuming that the HI has a spherical and isotropic distribution and that it is in hydrostatic equilibrium in the potential well of Sgr dIrr, the dynamical

⁶ <http://www.astro.rug.nl/~gipsy/>

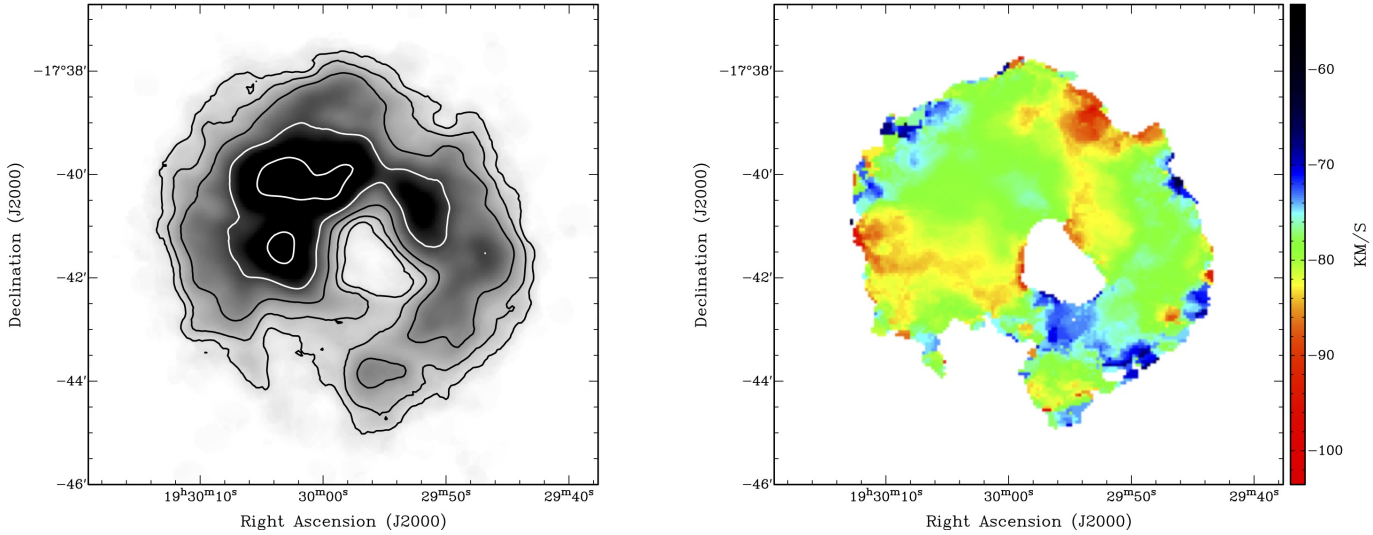


Fig. 13. Total HI map and velocity field obtained as a weighted average of the line profile. Both images have spatial resolution of $30'' \times 30''$, the contours in the HI maps are at $0.5, 1, 2, 4, 8 \times 10^{20} \text{ cm}^{-2}$.

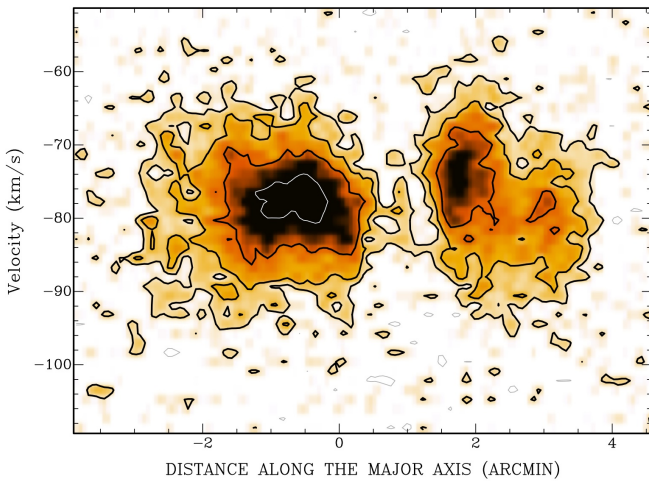


Fig. 14. HI position-velocity diagram taken along the optical major axis of Sgr dIrr, see Fig. 12, with position angle = 90° . Contours are at $-2, +2, 4, 8, 16$ in units of rms noise, and the spatial resolution is about $22''$, as in Fig. 12. The zero in x-axis corresponds to the optical centre of the galaxy, see Table 1.

mass ($M_{\text{dyn}} \sim 3r_G\sigma^2/G$; Ryan-Weber et al. 2008)⁷ would be about $5 \times 10^7 M_\odot$ for a gravitational radius $r_G \sim r_{\text{HI}} = 1 \text{ kpc}$. This would lead to a mass-to-light ratio $M_{\text{dyn}}/L_V \sim 9$, around the typical value for dwarfs of this luminosity (see M12, his Fig. 11, in particular).

6. Summary and discussion

We present new deep wide-field photometry of the isolated dwarf irregular galaxy Sagittarius. We do not see any sign of a metallicity gradient in the old- and intermediate-age population of the galaxy, and we confirm that this population has a much more extended distribution than young stars (age $\lesssim 1 \text{ Gyr}$).

⁷ In Paper I the rough estimate of the dynamical mass of VV124 was erroneously obtained with the same formula with a normalisation factor of 5 instead of 3. The guess estimates of the dynamical mass and mass-to-light ratio reported in that paper must therefore be reduced by a factor of $\frac{3}{5}$.

Our data allowed us to trace the structure of the galaxy out to much greater distances from the centre ($r_\epsilon \approx 5.0'$) and to much fainter surface brightness levels ($\mu_V \approx 30.0 \text{ mag/arcsec}^2$) than in any previous study. The major axis profile is fully consistent with a purely exponential model from $r_\epsilon \approx 200 \text{ pc}$ out to the least measurable point, at $r_\epsilon \approx 1600 \text{ pc}$, and available surface photometry indicates a flattening in the innermost $\sim 200 \text{ pc}$.

Surface density maps show that the stellar body of the galaxy is significantly elliptical with a boxy inner region surrounded by an elongated halo. This is significantly different from the morphology of the neutral hydrogen distribution, which is remarkably circular, it is off-centred with respect to the stellar body and displays multiple density peaks and holes (see also Young & Lo 1997).

The analysis of recent publicly available HI data showed that, while large scale gradients are seen in the velocity field, no clear sign of systemic rotation can be identified. Both a rotation amplitude lower than the HI velocity dispersion and chaotic motions induced by astrophysical mechanisms (e.g., star formation, gas in-/outflows) probably contribute to masking the underlying rotation signal, if any. Also the merging with another dwarf may have played a role in producing the disturbed HI morphology and velocity field (see, e.g., Deason et al. 2014; Fattahi et al. 2013, and references therein).

As a result, no robust estimate of the dynamical mass can be obtained from HI data. In this context, our new photometry can provide the targets for a kinematic follow up on RGB stars covering the whole extended body of the galaxy (as done, e.g., in Kirby et al. 2013, for VV124), aimed at obtaining an estimate of the mass relying on tracers whose motion only depends on the gravitational potential.

Acknowledgements. We are grateful to the referee, R.A. Ibata, for his useful suggestions. M.B., F.F., and A.S. acknowledge the financial support from PRIN MIUR 2010-2011 project ‘‘The Chemical and Dynamical Evolution of the Milky Way and Local Group Galaxies’’, prot. 2010LY5N2T. G. Battaglia gratefully acknowledges support through a Marie-Curie action Intra European Fellowship, funded from the European Union Seventh Framework Programme (FP7/2007-2013) under Grant agreement number PIEF-GA-2010-274151, as well as the financial support by the Spanish Ministry of Economy and Competitiveness (MINECO) under the Ramón y Cajal Program (RYC-2012-11537). This research made use of the SIMBAD database, operated at the CDS, Strasbourg, France. This research made use of the NASA/IPAC Extragalactic Database (NED) which is operated by the Jet Propulsion Laboratory, California Institute of Technology, under contract with the National Aeronautics and Space Administration.

References

- Ahn, C. P., Alexandroff, R., Allende, Prieto, C., et al. 2012, *ApJS*, 203, 21
- Barkana, R., & Loeb, A. 2001, *Phys. Rep.*, 349, 125
- Bellazzini, M. 2008, *Mem. Soc. Astrophys. It.*, 79, 440
- Bellazzini, M., Ferraro, F. R., & Pancino, E. 2001, *ApJ*, 556, 635
- Bellazzini, M., Ferraro, F. R., Origlia, L., et al. 2002, *AJ*, 124, 3222
- Bellazzini, M., Ferraro, F. R., Sollima, A., Pancino, E., & Origlia, L. 2004, *A&A*, 424, 199
- Bellazzini, M., Beccari, G., Oosterloo, T. A., et al. 2011a, *A&A*, 527, A58 (Paper I)
- Bellazzini, M., Perina, S., Galletti, S., Oosterloo, T. A. 2011b, *A&A*, 533, 37
- Bellazzini, M., Oosterloo, T., Fraternali, F., Beccari, G. 2013, *A&A*, 559, L11
- Bellazzini, M., Beccari, G., Fraternali, F., et al. 2014, *A&A*, 566, A44 (Paper II)
- Cesarski, D. A., Laustsen, S., Lequeux, J., Schuster, H.-E., & West, R. M. 1977, *A&A*, 61, L31
- Ciotti, L., & Bertin, G. 1999, *A&A*, 352, 447
- Correnti, M., Bellazzini, M., Dalessandro, E. et al. 2011, *MNRAS*, 417, 2411
- Dean, J. F., Warren, P. R., Cousins, A. W. J. 1978, *MNRAS*, 183, 569
- Deason, A., Wetzel, A., & Garrison-Kimmel, S. 2014, *ApJ*, 794, 115
- Dolphin, A. E. 2000, *PASP*, 112, 1383
- Fattahi, A., Navarro, J. F., Starkenburg, E., Barber, C., & McConnachie, A. W. 2013, *MNRAS*, 431, L73
- Ferraro, F. R., Messineo, M., Fusi Pecci, F., et al. 1999, *AJ*, 118, 1738
- Gallart, C., 2008, *ASP Conf. Ser.*, 390, 278
- Giallongo, E., Ragazzoni, R., & Grazian, A. 2008, *A&A*, 482, 349
- Greivich, J., & Putman, M. E. 2009, *ApJ*, 696, 385
- Gullieuszik, M., Rejkuba, M., Cioni, M. R., Habing, H. J., & Held, E. V., 2007, *A&A*, 475, 467
- Harris, W. E. 1996, *AJ*, 112, 1487
- Holtzman, J., Afonso, C., & Dolphin, A. 2006, *ApJS*, 166, 534
- Hunter, D. A., Ficut-Vicas, D., Ashley, T., et al. 2012, *AJ*, 144, 134
- Kazantzidis, S., Lokas, E. L., Callegari, S., Mayer, L., & Moustakas, L. A., *ApJ*, 726, 98
- Kirby, E. N., Cohen, J. G., & Bellazzini, M. 2012, *ApJ*, 751, 46
- Kirby, E. N., Cohen, J. G., & Bellazzini, M. 2013, *ApJ*, 768, 96
- Landolt, A. U. 1992, *AJ*, 104, 340
- Lee, M. G., & Kim, S. C. 2000, *AJ*, 119, 777 (LK00)
- Lelli, F., Verheijen, M., Fraternali, F. 2014, *A&A*, 566, A71
- Longmore, A. J., Hawarden, T. G., Webster, B. L., Goss, W. M., & Mebold, U. 1978, *MNRAS*, 183, 97
- Mateo, M. 1998, *ARA&A*, 36, 435
- Mayer, L., Kazantzidis, S., Mastrogiuseppe, C., & Wadsley, J. 2007, *Nature*, 445, 738
- McConnachie, A. 2012, *AJ*, 144, 4 (M12)
- Monelli, M., Hidalgo, S. L., Stetson, P. B., et al. 2010a, *ApJ*, 720, 1225
- Monelli, M., Gallart, C., Hidalgo, S. L., et al. 2010b, *ApJ*, 722, 1864
- Momany, Y., Held, E. V., Saviane, I., & Rizzi, L. 2002, *A&A*, 384, 393
- Momany, Y., Held, E. V., Saviane, I., et al. 2005, *A&A*, 431, 127 (M05)
- Rockosi, C. M., Odenkirchen, M., & Grebel, E. K. 2002, *AJ*, 124, 349
- Ryan-Weber, E. V., Begum, A., Oosterloo, T., et al. 2008, *MNRAS*, 384, 535
- Sanna, N., Bono, G., Stetson, P. B., et al. 2010, *ApJ*, 722, L244
- Saviane, I., Rosenberg, A., Piotto, G., Aparicio, A. 2000, *A&A*, 355, 966
- Saviane, I., Rizzi, L., Held, E. V., Bresolin, F., & Momany, Y. 2002, *A&A*, 390, 59
- Sawala, T., Scannapieco, C., Maio, U., & White, S. 2010, *MNRAS*, 402, 1599
- Sawala, T., Scannapieco, C., & White, S. 2012, *MNRAS*, 420, 1714
- Schlafly, E., & Finkbeiner, D. P. 2011, *ApJ*, 737, 103
- Schlegel, D. J., Finkbeiner, D. P., & Davis, M. 1998, *ApJ*, 500, 525
- Sérsic, J. L. 1968, *Atlas de Galaxias Australes* (Cordoba, Argent.: Obs. Astron.)
- Stetson, P. B. 1987, *PASP*, 99, 191
- Stetson, P. B. 1994, *PASP*, 106, 250
- Teyssier, M., Johnston, K. V., & Kuhlen, M. 2012, *MNRAS*, 426, 1808
- Tolstoy, E., Hill, V., & Tosi, M. 2009, *ARA&A*, 47, 371
- Vansevicius, V., Arimoto, N., Hasegawa, T., et al. 2004, *ApJ*, 611, L93
- Young, L. M., & Lo, K. Y. 1997, *ApJ*, 490, 710
- Weisz, D. R., Dolphin, A. E., Skillman, E. D., et al. 2014, *ApJS*, 789, 147